Corrosion behavior of various conductive materials in Sb3Sn7 alloy at 450 °C

Tianru Zhang [a], Renate Fetzer [a,*], Annette Heinzel [a], Alfons Weisenburger [a], Chongchong Tang [b], Michael Stüber [b], Georg Müller [a]

[a] *Institute for Pulsed Power and Microwave Technology (IHM), Karlsruhe Institute of Technology (KIT), Hermann-von-Helmholtz-Platz 1, 76344 Eggenstein-Leopoldshafen, Germany*
[b] *Institute for Applied Materials (IAM), Karlsruhe Institute of Technology (KIT), Hermann-von-Helmholtz-Platz 1, 76344 Eggenstein-Leopoldshafen, Germany*

A R T I C L E   I N F O

A B S T R A C T

Sb-Sn alloys are attractive positive electrode materials for liquid metal batteries. In this work, the corrosion behavior of three steels (f/m steel T91, austenitic steels SS304 and SS316L), one Fe-Co-Ni alloy (4J29 Kovar), molybdenum, and three MAX-phase coatings (Cr_2AlC, Ti_2AlC, Ti_3AlC_2) is investigated in static exposures to liquid Sb_3Sn_7 alloy at 450 °C for 750 h in oxygen-poor conditions. The results reveal unacceptably high corrosion rates in the range 0.5 to 1.3 μm/h for the Fe-based alloys, while Mo and MAX-phases show promising corrosion resistance with corrosion rates below 0.1 mm/a despite a small arsenic impurity of the liquid metal.

1. Introduction

Liquid metal batteries (LMBs) are researched as potential large-scale stationary energy storage systems to compensate the intermittence of renewable energy supply [1–5]. Due to the liquid state of both electrodes and the electrolyte, no dendrite formation and degradation upon cycling occurs, which promises high cycle life. In addition, the fast reaction kinetics at the electrode-electrolyte interfaces enable charging and discharging at high current density. Finally, good scalability and an easier temperature management compared with conventional large-scale batteries make liquid metal batteries attractive candidates for low-cost grid-scale electrical energy storage.

An LMB is composed of a low-density metal with low electronegativity (Li, Na, Mg, Ca) used as negative electrode, a high-density metal with high electronegativity (Pb, Sb, Bi) as positive electrode, and an electrolyte, typically a molten salt, that separates the two electrodes and conducts the ions of the metal chosen as negative electrode. Most studies on LMBs use Li as negative electrode due to its excellent electrochemical properties, high energy density, low melting temperature, and low solubility in alkali metal salts. As an alternative, Na is researched because of its high abundance, low cost, and environmental advantages. The high self-discharge of Na-based LMBs can be reduced by using the molten salt mixture LiCl-NaCl-KCl (eutectic, melting temperature ~350 °C) as electrolyte [6,7]. Among the candidate heavy metals for the positive electrode, antimony (Sb) is regarded as the most promising one owing to its low cost and high cell voltage when coupled with a negative electrode. However, the high melting temperature of Sb (631 °C) requires an undesirably high operating temperature of the LMB cell, which results in increased self-discharge and corrosion. Alloying Sb with Pb, Bi, or Sn can significantly decrease the melting point of the positive electrode and thus the cell operating temperature without a decrease in cell voltage [3,4]. Due to the potential environmental concerns of large-scale application of lead, Sn and Bi are the preferred choice [4,8]. Recently, most studies focused on Sb-Sn alloys, especially when combined with Li as negative electrode, due to the high abundance and lower cost of Sn compared with Bi.

One major drawback of Sb-Sn alloys is their aggressiveness towards structural materials that may serve as positive current collector (PCC) in an LMB. Corrosion of the PCC material not only brings safety concerns on the long service lifetime of LMBs. Diffusion of dissolved constituents of PCC materials into the liquid positive electrode and alloying with the cell active components could also have adverse effects on the cell performance, including undesirable side-reactions, increased cell internal resistance, and reduced cell capacity [9–11].

Liquid metal corrosion in general challenges the development not only of LMBs but also of other technologies where liquid metals are considered, e.g., as coolants in nuclear power plants [12] or as heat transfer fluids in concentrating solar power systems [13–15].

---

* Corresponding author.
  E-mail address: renate.fetzer@kit.edu (R. Fetzer).

Application in these fields triggered intensive research on corrosion of structural materials in liquid metals and the main corrosion mechanisms between solid structural materials and liquid metals have been established [13,15,16]. The principal identified corrosion mechanisms include (1) dissolution of some or all constituents of the solid material into the liquid metal, (2) dissolution and penetration of the liquid metal into the structural material, and (3) selective reactions, formation of intermetallic compounds and solid solutions. The conventional corrosion protection strategy is to provide an appropriate amount of oxygen in the liquid metal (e.g., 10^{-6} wt% oxygen dissolved in liquid Pb or Pb-Bi eutectic) to in-situ form protective oxide layers on the surfaces of the structural materials [17,18]. Hereby, Al-rich oxide scales (ideally α-Al_2O_3) are preferable over Fe-based oxides due to their slow growth rate, high density, and high mechanical stability. Furthermore, the formation of Al-oxide requires less oxygen dissolved in the liquid metal than the formation of Fe- or Cr-based oxides. Thus, the use of alumina-forming materials or alumina-forming coatings can significantly enhance the corrosion resistance, especially at high temperature or in oxygen-poor liquid metal environment. However, corrosion mitigation by a controlled in-situ growth of protective oxide scales, no matter whether based on Fe, Cr, or Al, requires a certain minimum oxygen concentration and/or oxygen supply. Therefore, this mitigation strategy does not work in low-oxygen or oxygen-free environment as required for instance in LMBs, for CO_2-free thermal decomposition of methane [15], or when sodium or lithium is present.

Regarding corrosion in Sb-Sn alloys, most previous studies focused on corrosion in pure liquid antimony or in pure liquid tin. Armco iron, cast iron, low-carbon steel (0.13 wt% C), and cast steel were investigated and proven to have poor resistance against corrosion by liquid antimony (i.e., at temperatures of 630 °C and above) due to the formation of Fe-Sb compounds [16,19,20]. Chromium and nickel are excluded from consideration as container materials for liquid antimony due to their appreciable solubility in liquid antimony at low temperatures [16,20]. Tin, on the other hand, forms intermetallic phases with Fe, Ni, and Cr and is therefore the most aggressive liquid metal towards steels or Ni-based alloys [21–24]. Tin corrodes stainless steel heavily already at a temperature of only 300 °C [21,22]. Nickel exhibits appreciable solubility in liquid tin at low temperatures [16,20], while chromium shows no signs of corrosion attack by liquid tin at the melting point of tin (231.9 °C) and may behave well at considerably higher temperatures [16,20]. Even niobium (Nb) and molybdenum (Mo), which are regarded as resistant against most other liquid metals due to their generally low solubility and which have been suggested for use with liquid tin [16,20], may substantially corrode in the presence of liquid tin as a result of the formation of intermetallic compounds [16,20, 23,25].

Studies on the combined effects of antimony and tin on corrosion, i. e., corrosion in Sb-Sn alloys, emerged only recently, most of them related with corrosion of candidate PCC materials in Li‖Sb–Sn LMBs. Liu et al. investigated static corrosion of Fe, Cr, Ni, and several steels in Sb_4Sn_6 at 500 °C for a rather short time (160 h) [26]. The results showed that Cr possesses the lowest corrosion rate among Fe, Ni, and Cr, while Ni has the highest corrosion rate. For the steels, higher Ni contents were found to be detrimental, while a higher Cr content has a beneficial effect on the corrosion behavior. Corrosion rates were in the range 0.2–1 μm/h for the steels. Cui et al. studied the corrosion of SS304 [11] and of Ti, Mo, and W [27], both in static exposures to Sb_4Sn_6 alloy at 500 °C and when used as PCC in operating Li‖Sb–Sn cells. Regarding static corrosion, the studies showed that an Fe-Sb corrosion layer forms on SS304. The corrosion rates of the pure metals rank Ti>Mo>W with 0.012 μm/h, 0.008 μm/h, and 0.002 μm/h, respectively. Much stronger corrosion of all materials was observed when used as PCC in a Li‖Sb–Sn cell during cycling. In case of W, this was attributed to erosion and cavitation corrosion, while all other materials suffered mainly from the action of Li in the positive electrode. Thus, corrosion of these materials in Na-based LMBs is still an open issue.

In the present work, we focus on static corrosion tests in oxygen-poor liquid Sb-Sn alloys. We investigate five different metallic bulk materials (ferritic steel T91, austenitic stainless steels SS304 and SS316L, Kovar 4J29 alloy, and Mo metal) and three MAX-phases (Cr_2AlC, Ti_2AlC, Ti_3AlC_2) coated on Al_2O_3-substrates. Austenitic stainless steels are the most common and most widely used structural materials. Due to the expected strong dissolution of Ni, also the 9Cr-1Mo ferritic steel T91 was tested. Although Mo was found not to survive operating conditions of Li‖Sb–Sn cells [27], it is generally known for its good corrosion resistance and better mechanical properties compared with W and may survive the conditions in Na‖Sb–Sn cells. The selection of the Kovar alloy is motivated by the design of an LMB cell, in particular the negative current collector (NCC), which is insulated from the PCC by a gas-tight dielectric break [9]. Kovar alloy (nickel-cobalt ferrous alloy) is regarded as one of the appropriate candidates for NCC due to its similar thermal expansion properties as ceramic materials [28,29].

MAX-phases are selected because of their unique combination of metallic and ceramic properties, which enables applications in harsh environments where metals fail due to material compatibility issues and ceramics cannot provide electrical conductivity. MAX-phases are nano-layered, hexagonal, ternary carbides and nitrides with the general formula $M_{n+1}AX_n$ (n = 1 to 3), where M is a transitional metal, A is an A-group element from IIIA or IVA group and X is either carbon or nitrogen. The unique nano-laminated crystal structure of MAX-phases endow them with a distinctive combination of metallic and ceramic properties, including high electrical and thermal conductivity, excellent machinability, low thermal expansion coefficients, and good corrosion resistance against chemical attack [30,31]. Except for some parasitic secondary phases due to a non-perfect production process in the early development of these materials, MAX phases have shown excellent corrosion resistance in oxygen-poor lead-bismuth eutectic [32,33]. Motivated by these promising results, the three MAX-phases coatings Cr_2AlC, Ti_2AlC, Ti_3AlC_2 were selected because of their mature fabrication process and good corrosion behavior [34,35].

Specimens of the selected eight different materials are exposed for 750 h at 450 °C to the liquid metal alloy Sb_3Sn_7 in Ar5%H$_2$ atmosphere in order to evaluate their potential to be applied as PCC in LMB cells, in particular in Na-based LMBs. The alloy composition Sb_3Sn_7 is selected due to its lower melting point compared with Sb_4Sn_6, which also allows a lower operating temperature of 450 °C for an LM battery. Although the selected materials and exposure conditions are motivated by their potential application in (Na-based) LMB cells, the static exposures make the results applicable to all fields of liquid metal technology in oxygen-poor conditions.

2. Materials and methods

2.1. Materials

Sn was delivered by HMW Hauner GmbH & Co. KG with the granular size of 2–4 mm and a purity of 99.99%. Sb was delivered by Haines & Maassen Metallhandelsgesellschaft GmbH with a purity of 99.65% and a granular size of 1–10 mm. The alloy Sb_3Sn_7 was obtained by mixing the individual heavy metals Sb and Sn in their granular forms in alumina crucibles and melting under controlled atmosphere, see below. The final Sb-Sn alloy contained a small, hardly detectable (<0.1%) impurity from arsenic (As), which most probably stemmed from an impurity of the Sb raw material. Arsenic is a very typical impurity of Sb [36].

The test specimens in this work were Mo metal (Plansee SE), T91 ferritic-martensitic steel (EUROTRANS-DEMETRA, [37]), 304 austenitic stainless steel (SS304), 316 L austenitic stainless steel (SS316L) (EUROTRANS-DEMETRA, [37]), 4J29 Kovar alloy (Dongguan Saijing Special Alloy Co. Ltd.) and three MAX-phase coatings (Cr_2AlC, Ti_2AlC, and Ti_3AlC_2) on Al_2O_3-substrate (IAM-AWP, KIT).

The compositions of the steels and Kovar alloy are listed in Table 1. The MAX-phase coatings were synthesized by a two-step method,

Table 1
Composition of steel and alloys test specimens (in wt%). Data for T91 and SS316L are taken from [37], data for SS304 and Kovar 4J29 are measured by SEM-EDS.

Specimen	C	Co	Cr	Ni	Mn	Mo	Al	Si	Fe
T91	0.10	/	8.99	0.11	0.38	0.89	0.015	0.22	Bal.
316 L	0.02	/	16.73	9.97	1.81	2.05	0.02	0.67	Bal.
304		/	18.7	8.2	1.6	/	/	0.5	Bal.
4J29		17.6	/	28.1	0.1	/	/	0.4	Bal.

deposition of nanoscale elemental M/C/Al multilayers by magnetron sputtering and the subsequent ex-situ thermal annealing in argon atmosphere. The coating thicknesses were ~3 µm. More details on the coating synthesis can be found elsewhere [38]. Although high purity Ar (6.0) atmosphere was used for thermal annealing, some oxygen was introduced into the superficial layer of the MAX-phase coatings during annealing by diffusion and preferential oxidation of Al [39].

All specimens were cut into appropriate size to fit into the sample holder (Fig. 1). Then, all test materials except for the three MAX-phase coatings were ground by sandpaper with a grit size of 800 and 1200, successively. Finally, the specimens were fixed to an alumina holder by Mo-wires, see Fig. 1, and transferred into a glovebox.

2.2. Alloy preparation and exposure tests

The alloy preparation and corrosion tests were performed in the corrosion test facility COSTA (COrrosion test stand for STagnant liquid Alloys) [22]. It consists of a quartz tube inside a furnace that regulates the isothermal condition for the exposure test. The quartz tube is connected with a gas control system to adjust and continuously control the gas atmosphere.

For alloying and pre-conditioning of the liquid Sb_3Sn_7 alloys, alumina crucibles were filled with ca. 100 g of Sb and Sn granules in the required ratio and placed inside the quartz tube at room temperature. Then, the quartz tube was purged with a flow of Ar5%H$_2$ gas (purity: argon 6.0 and hydrogen 6.0) for 2 days. After reaching an oxygen content of 10^{17} ppm or lower in the gas phase leaving the quartz tube, the temperature inside the quartz tube was raised up to 700 °C and hold there for several hours to melt the heavy metal granules (note the high melting point of Sb of 631 °C) and to remove all remaining oxides from the Sb-Sn alloys. Finally, the temperature was decreased to the test temperature of 450 °C.

For loading and unloading the specimens, a glovebox with the specimens was pre-conditioned with Ar5%H$_2$ gas and connected to the quartz tube to maintain the atmosphere inside the tube. Each specimen was put in a separate crucible containing the pre-conditioned liquid Sb-Sn alloy. Once back in the quartz tube inside the furnace, the crucibles with Sb_3Sn_7 and the specimens were held isothermally at 450 °C for

750 h under a continuous flow of Ar5%H$_2$ (flow rate 100 mL/min) and permanent control of the atmosphere. The measured oxygen content in the gas phase leaving the quartz tube was in the range 10^{19} to 10^{17} ppm during the entire exposure test. This value was obtained by an oxygen sensor heated to 750 °C and corresponds to a water vapor to hydrogen ratio p_{H_2O}/p_{H_2} of 0.002 to 0.02 and to an oxygen partial pressure of 10^{36} to 10^{34} bar in the test section.

2.3. Post-test analysis

After 750 h exposure, the specimens were extracted from the liquid Sb-Sn alloy and cooled down to room temperature under controlled atmosphere in the glovebox. The immersed part of all metallic specimens was more or less covered by a layer of Sb-Sn alloy. In contrast, no attachment of liquid Sb-Sn alloy was visible on the three MAX-phases.

All metallic specimens were cut, embedded in resin, ground and polished to a diamond size of 1 µm. Scanning electron microscopy (SEM) with energy dispersive X-ray spectrometry (EDS) was used for the examination. Considering that no Sb-Sn alloy stuck on the surfaces of the three MAX-phases, only their surface was observed and examined.

3. Results

Post-test SEM/EDS analysis of the specimens revealed that As from the small impurity of the Sb-Sn alloy had accumulated in significant amounts in some specific locations of some specimens. In order to clarify its effect on the individual corrosion behaviors, the As concentration and distribution was measured for all specimens.

3.1. Fe-Cr steel

Fig. 2 shows the secondary electrons (SE) SEM image of a cross-section of T91 ferritic steel after 750 h exposure to liquid Sb_3Sn_7. The Sb-Sn alloy attached on the steel surface and reacted with the steel, which lead to the formation of a rather homogeneous corrosion layer throughout the entire surface of the T91 specimen. The corrosion depth is in the range of 200 µm to 400 µm, which corresponds to a corrosion rate of up to 0.53 µm/h.

The back-scattered electrons (BSE) SEM image and EDS element mapping images of the T91 cross-section after exposure in liquid Sb_3Sn_7 with a higher magnification are shown in Fig. 3. It can be seen that T91 is

Fig. 1. Cut alumina crucible with a sample fixed to an alumina holder by Mo-wires.
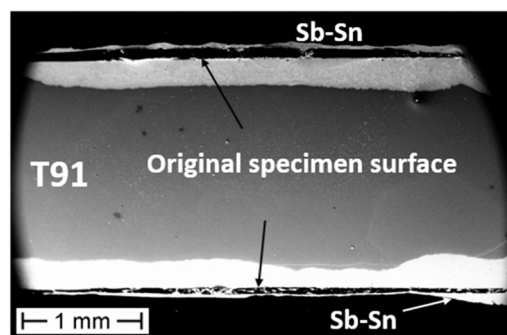
Fig. 2. SE-SEM image of cross-section of T91 ferritic steel after 750 h exposure in liquid Sb_3Sn_7 at 450 °C.

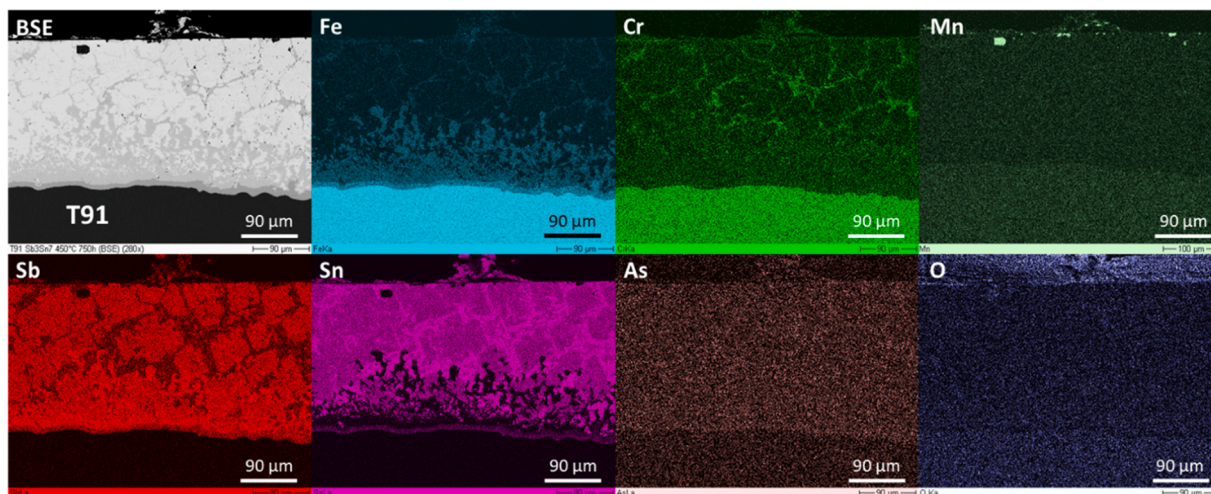**Fig. 3.** BSE-SEM image and EDS element mapping images of cross-section of T91 ferritic steel after 750 h exposure in liquid Sb_3Sn_7 at 450 °C.

depleted in both Fe and Cr in the corroded region, while Sb and Sn show apparent penetration. However, the distribution of the elements in the corrosion attack is not homogeneous. Cr has a higher concentration along lines that most probably correspond to the prior austenite grain boundaries in the martensitic microstructure. Sn is enriched in close vicinity of these Cr-rich paths, while Sb is mainly found further away from them. Towards the corrosion front, the concentration of Sn declines. The dark spots close to the sample surface are Mn-, Mo-rich precipitates. The As concentration is low and rather homogeneous in the entire corrosion attack. Additionally, a very low oxygen signal is detected mainly in the resin and in the uncorroded T91, which clearly indicates that it originates from oxidation of the specimen cross section after its preparation.

The line scan in Fig. 4 shows a more detailed analysis of the corroded area. Directly at the corrosion front, a layer of about 10 μm thickness is found that appears dark in the BSE signal and is marked as zone 1 in Fig. 4. This layer has a distinctly higher Fe content compared with the rest of the corroded region. In this layer, the Fe concentration is about 50 at%, the Sb content decreases from ~30 to ~20 at% towards the corrosion front, and the concentration of Sn increases from ~13 to ~20 at%. The region directly adjacent to the layer at the corrosion front, medium-dark in the BSE-SEM image and denoted as zone 2, is characterized by an intermediate Fe content (~28 at%), a rather high Sb content (~60 at%), and a very low Sn content (<5 at%). This region transitions via a patchy boundary to an extended corrosion region (zone 3) that appears bright in the BSE-SEM image and consists basically of Sb (~50 at%) and Sn (~40 at%) only. As mentioned above, a different composition is found along prior austenite grain boundaries (zone 4). Here, Fe and Cr show a local enrichment with ~10 at% each, together with ~5 at% As. These spots are directly surrounded by a very high Sn

concentration (~80 at%). Except for the mentioned small local enrichment to ~5 at% along grain boundaries, the As concentration is < 2 at% throughout the entire corrosion attack.

Remarkable is that the borders between the described layers and regions are clearly pronounced, i.e., the composition does not change gradually but in steps. In particular, the Fe content sharply decreases at the corrosion front from the specimen's bulk value to ~50 at%, then in a second step to ~28 at%, and finally to an amount < 5 at%. This stepwise change in composition indicates the formation of intermetallic phases. According to the binary phase diagrams of Fe-Sb and Fe-Sn, several stable intermetallic phases exist at 450 °C, namely ε-FeSb, $FeSb_2$, FeSn, and $FeSn_2$ [40]. In the ternary system Fe-Sb-Sn at 200 °C, the similarity of Sb and Sn leads to a significant substitution of each other in the Fe-Sb and Fe-Sn compounds at constant Fe content [41]. For low Fe contents, additionally the binary Sb-Sn phase β exists with wide homogeneity range. Taking the data at 200 °C as reference, the composition in the first layer at the corrosion front of T91 (zone 1 in Fig. 4) indicates the phases ε+$FeSn_2$ +β at the front, gradually transitioning to the phases ε+$FeSb_2$ +β at the end of this layer. The second region (zone 2) with main contributions from Sb and Fe in the atomic ratio 2:1 indicates dominant presence of the intermetallic phase $FeSb_2$.

3.2. Fe-Cr-Ni steels

The corrosion of SS316L by Sb_3Sn_7 after 750 h is shown in a typical cross section in Fig. 5. Compared with T91, the corrosion attack is less homogeneous. The corrosion depth is around 200 μm on average, but can also reach ~600 μm, corresponding to a maximum corrosion rate of 0.8 μm/h.

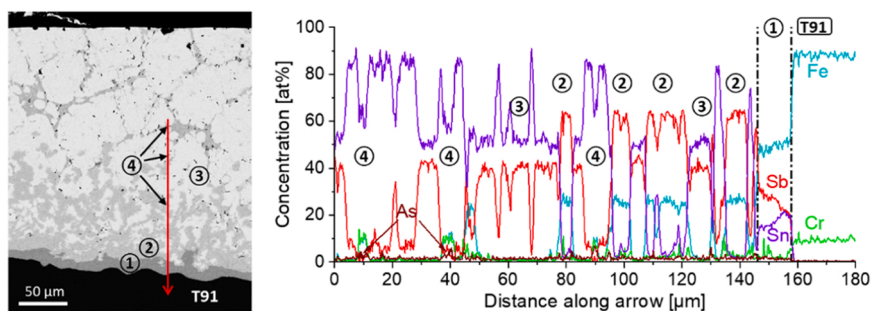The BSE and EDS element mapping images of the cross-section of

Fig. 4. Line scan through corroded region of T91, where ① marks the dark layer at the corrosion front, followed by the medium-dark Sn-poor region ②. The bright extended corrosion region ③ is interrupted by the Cr-rich corrosion along prior austenite grain boundaries ④.
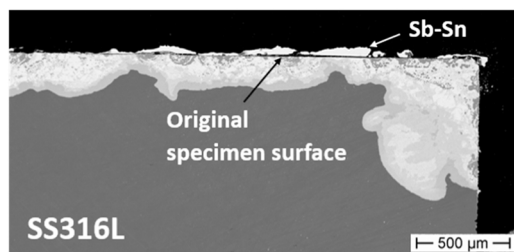
Fig. 5. BSE-SEM image of cross-section of SS316L after 750 h exposure in liquid Sb$_3$Sn$_7$ at 450 °C.

SS316L after exposure, Fig. 6, show depletion of all main constituents (Fe, Cr, Ni) of SS316L in the corroded region as well as penetration of Sb and Sn. Qualitatively different regions can be identified within the corrosion attack. At the corrosion front, there is a 20–50 μm thick region with a lower amount of Sn and a higher content of Fe compared with the rest of the corroded area. Except for this 20–50 μm thick region, the corrosion attack is characterized by an accumulation of Cr at the sample surface and in Cr-rich areas that appear complementary to Sb- and Sn-rich regions. Ni is homogeneously depleted in the entire corroded region of the steel, while it is enriched to similar concentrations in the Sb-Sn alloy attached on the specimen surface. High concentrations of As are found at the Cr-rich spots; the rest of the corroded area shows very low As content. As for T91, a low intensity oxygen signal is found mainly in the resin and the uncorroded steel, which is attributed to oxidation of the specimen cross section after its preparation.

The corresponding line scan through the corrosion attack reveals the composition in different regions quantitatively, see Fig. 7. The layer formed at the corrosion front (zone 1) possesses a constantly high Fe content of ~45 at% and Cr content of ~8 at%, while the Sb content decreases from ~30 to ~20 at% towards the corrosion front and the Sn content increases from ~10 to ~20 at%. The Ni content is below 5 at%. Except for the higher thickness, these features are the same as in the first layer of the corrosion attack of T91 described above. As for T91, also the composition of SS316L indicates a gradual transition from the phases ε+FeSn$_2$ +β at the corrosion front to the phases ε+FeSb$_2$ +β at the end of this first layer.

In the adjacent second region (zone 2) of the corrosion attack of SS316L, the Fe content is ~28 at% and the Sb content is ~60 at%, while Cr, Sn, and Ni show low concentrations. These are, again, concentrations very close to the ones observed for T91 in zone 2 and indicate a main contribution from the intermetallic phase FeSb$_2$. SS316L contains roughly equal amounts of Sb and Sn in zone 3, which is again similar to

T91 and indicates the Sb-Sn phase β. In contrast to T91, SS316L shows Cr-rich patches close to the specimen surface (zone 4), with ~40 at% Cr and an even higher concentration of As (~47 at%).

The corrosion behavior of SS304, the second investigated Fe-Cr-Ni steel, is presented in Figs. S1-S3 in the Supporting Information. For SS304, the corrosion attack is even more inhomogeneous than for SS316L, with a higher maximum corrosion depth of ~1 mm, see Fig. S1. The corroded areas show the same internal structure as SS316L (see elemental mapping shown in Fig. S2), where the compositions of the distinct layers and regions agree with the compositions found for SS316L (see respective line scan in Fig. S3). Instead of the extended enrichment of Cr at the surface, however, a much thinner Cr-rich layer is found at the surface and some small Cr-rich precipitates are observed in the bulk of the corroded region. As for SS316L, very high concentrations of As are found in the Cr-rich spots, while the low oxygen signal stems from oxidation of the cross-section after the exposure experiment.

The similarity of the compositions in the corroded regions of the Fe-Cr steel T91 on the one hand and the Fe-Cr-Ni steels SS304 and SS316L on the other hand is enabled by the strong depletion of Ni in the corroded regions of the austenitic steels. Ni has a significant solubility in liquid Sn (~1 at% at 450 °C). In addition, it can form solid compounds with both Sb (NiSb$_2$, NiSb, etc.) and Sn (Ni$_3$Sn$_4$, Ni$_3$Sn$_2$, Ni$_3$Sn), which results in a continued dissolution even after reaching saturation in the liquid phase. In regions with Ni depletion due to dissolution into the adjacent Sb-Sn alloy, the austenitic steels are weakened and both Sb and Sn can penetrate more easily. This explains the inhomogeneous corrosion attack with locally enhanced corrosion rates up to 0.8 μm/h (SS316L) respectively 1.3 μm/h (SS304) of austenitic Fe-Cr-Ni steels in contrast to the more homogeneous corrosion rate of 0.3–0.5 μm/h observed for the ferritic Fe-Cr steel T91.

3.3. Fe-Co-Ni alloy

After 750 h exposure to Sb$_3$Sn$_7$, the 4J29 Kovar alloy specimen entirely lost its original surface, see Fig. 8. The corrosion depth is rather homogeneous and lies in the range 300 to 400 μm, which translates into a maximum corrosion rate of 0.53 μm/h.

From the BSE image and the EDS element mapping images of the Kovar specimen's cross-section shown in Fig. 8, it is observed that the material adjacent to the unaffected Kovar contains Sb, Sn, Fe, Ni, and Co distributed in patches of different compositions. The concentration of As is very low in the entire corrosion products.

The line scan shown in Fig. 9 reveals the composition in some of the patches of the attached alloy. The dark patch (zone 1) directly adjacent to the undisturbed Kovar alloy shows equally high amounts of Fe and Sb
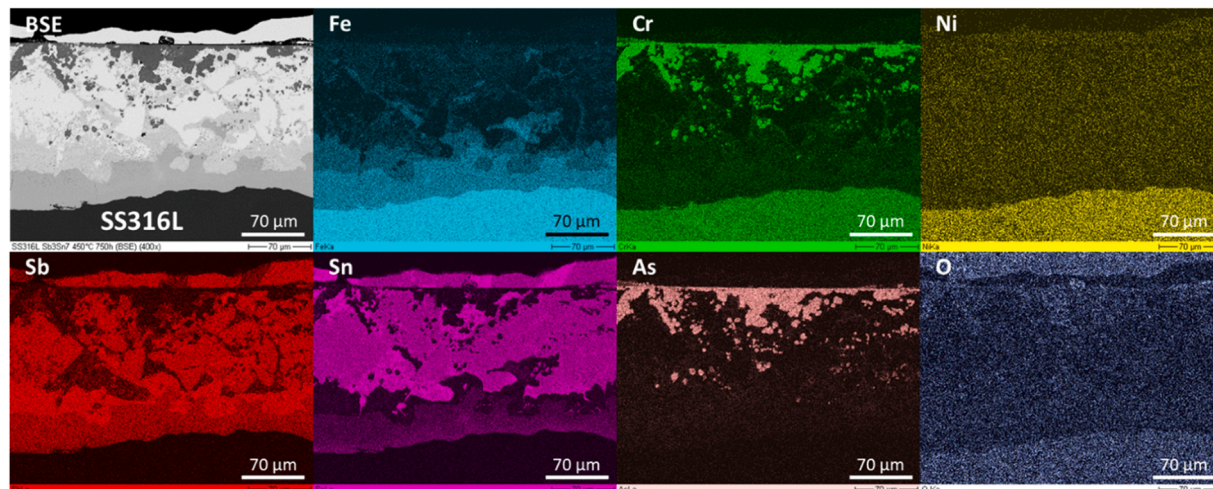

Fig. 6. BSE-SEM image and EDS element mapping images of cross-section of SS316L after 750 h exposure in liquid Sb$_3$Sn$_7$ at 450 °C.
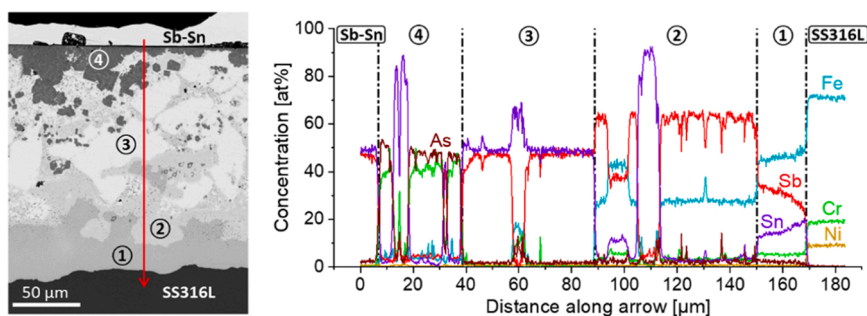
Fig. 7. Line scan through corroded region of SS316L, where ① is the layer at the corrosion front, ② is the adjacent corrosion region with intermediate Fe content, ③ is the corrosion region that shows the brightest signal, and ④ marks As-Cr-rich patches.
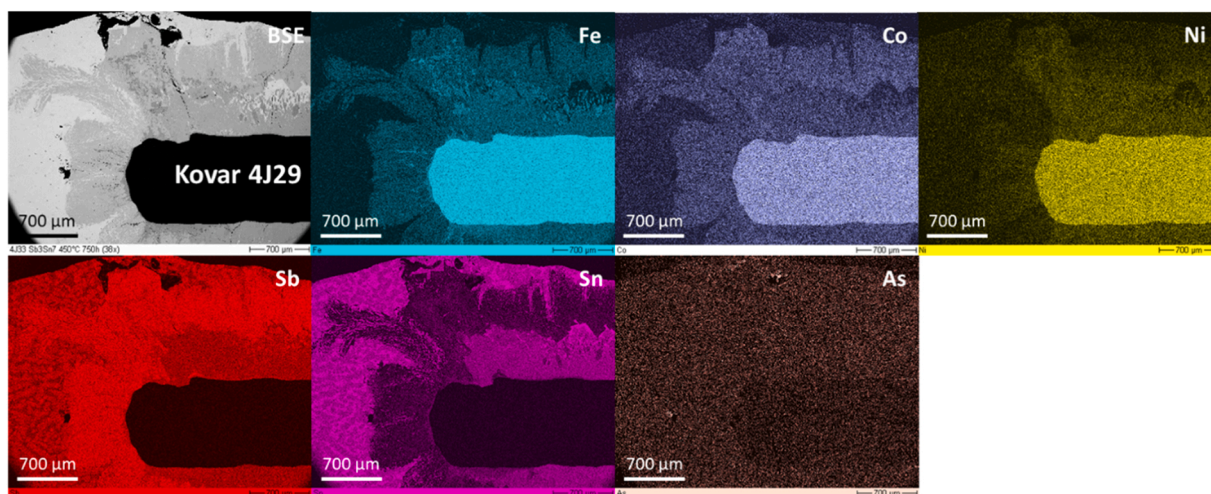

Fig. 8. BSE-SEM image and EDS element mapping images of cross-section of 4J29 Kovar alloy after 750 h exposure in liquid Sb_3Sn_7 at 450 °C.
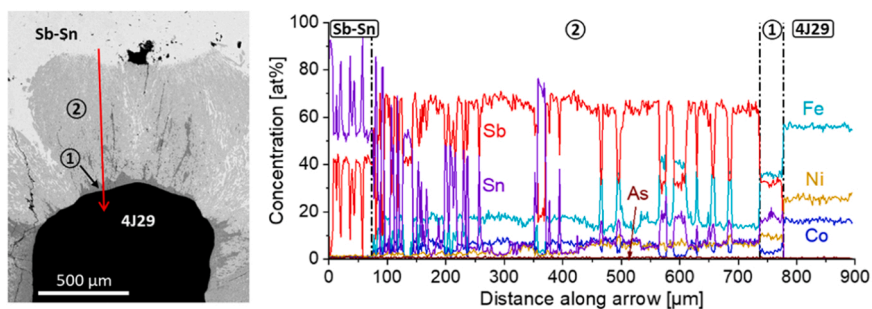

Fig. 9. Line scan through corrosion products of 4J29 Kovar alloy, where ① is the dark patch formed at the corrosion front and ② is an extended region with intermediate brightness in the BSE-SEM image.

(~35 at% each), ~10 at% Sn, and ~12 at% Ni. The lowest amounts are found for Co with ~5 at%. Medium dark patches (zone 2) have ~65 at% Sb, ~15 at% Fe, and 5–10 at% Sn, Ni, and Co. This matrix is decorated by many small spots, either with composition as in zone 1 or with roughly equal amounts of Sb and Sn, as was found in zone 3 of Fe-Cr-Ni steels, Fig. 7. Bright regions (marked as Sb-Sn) have an average composition close to the original alloy Sb_3Sn_7 with very low contributions from the alloying elements of 4J29 Kovar. The concentration of As is < 1 at% throughout the entire measurement, which is significantly lower than the maximum As contents found in the corrosion attack of Fe-Cr and Fe-Cr-Ni steels described above. The lower As content might be explained by the absence of Cr in Kovar alloy.

As noted above for the steels, the stepwise changes in composition indicate the formation of intermetallic phases. In case of Kovar, the dark

patches (zone 1 in Fig. 9) may contain the intermediate phases ε+FeSb₂ +β and the adjacent patches (zone 2) the phases ε+FeSb₂ +Sb+β.

The strong corrosion attack of 4J29 Kovar alloy in liquid Sb_3Sn_7 is most probably caused by the high Co and Ni contents of Kovar. Similar to Ni, also Co has a significant solubility of ~1 at% in Sn at 450 °C and can form solid compounds with Sn and Sb ($CoSn_2$, CoSn, $CoSb_3$, $CoSb_2$, CoSb). Thus, the dissolution of both Co and Ni into the adjacent liquid Sb-Sn alloy drives the corrosion of 4J29 Kovar.

3.4. Mo metal

The corrosion of Mo by Sb_3Sn_7 is very mild, see overview BSE image of the specimen's cross-section in Fig. 10. Nevertheless, the Sb-Sn alloy attached on the surface of the specimen, which indicates some reaction
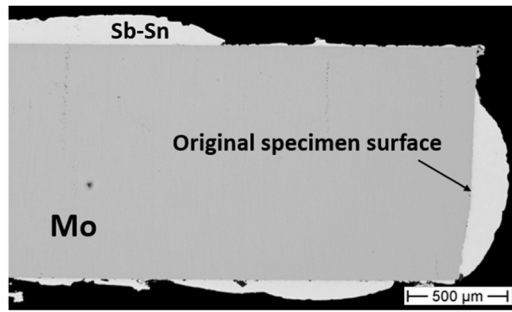
Fig. 10. BSE-SEM image of cross-section of Mo metal after 750 h exposure in liquid Sb_3Sn_7 at 450 °C.

between the alloy and Mo.

The more detailed analysis shown in Fig. 11 reveals a low concentration of Mo in the attached Sb-Sn alloy. In addition, some local corrosion attacks are found along the specimen surface, where Sb and Sn penetrated up to a depth of ~5 μm (corrosion rate 0.007 μm/h). In these confined spots a high concentration of As is found. As revealed by line scans, the concentration of As (~30 at%) even exceeds the concentration of Sb (~10 at%) and Sn (<5 at%) at the corrosion front, which indicates that As is predominantly responsible for these local corrosion attacks.

3.5. MAX-phases

Fig. 12(a) shows an SE image and EDS elemental mapping images of the surface of Ti_2AlC after exposure to liquid Sb_3Sn_7. The specimen surface is decorated with small bright spots, which are identified as droplets of the Sb-Sn alloy. In areas not covered by attached Sb-Sn droplets, no sign of corrosion can be found, see SE images with higher magnification shown in Fig. 12(b). Neither are any holes observed nor is any signal from Sb or Sn detected in the X-ray spectrum of the EDS analysis, i.e., neither Sb nor Sn penetrated into the MAX-phase (Fig. 12 (b)). The other two MAX-phases Ti_3AlC_2 and Cr_2AlC, presented in Figs. S4 and S5 of the Supporting Information, show the same excellent corrosion resistance as Ti_2AlC after exposure in liquid Sb_3Sn_7: Despite some small droplets of Sb-Sn alloy attached on the surface, no signs of corrosion are detectable on the specimens' surfaces.

EDS point measurements on the MAX-phase surfaces reveal an oxygen content that increases with decreasing accelerating voltage and, thus, decreasing penetration depth of the beam electrons into the

sample. This effect is largest for Cr_2AlC with an O content enriched by a factor of 1.23 (10 kV) and 1.34 (8 kV), respectively, compared with the bulk values obtained at 15 kV or 20 kV. The oxygen enrichment at the sample surface is combined with a slight increase of the Al content (factor 1.18) and indicates the presence of a thin (< 100 nm) Al-rich oxide scale.

4. Discussion

In this work, the corrosion behavior of five metallic bulk materials (T91 ferritic steel, SS304 and SS316L austenitic stainless steel, 4J29 Kovar alloy, Mo metal) and three MAX-phase coatings (Cr_2AlC, Ti_2AlC, Ti_3AlC_2) in oxygen-poor liquid Sb_3Sn_7 at 450 °C with the duration of 750 h was investigated with the aim of evaluating their potential to be applied as PCC in (Na-based) LMBs. An arsenic contamination of the Sb-Sn alloy provided additional insights regarding its effect on corrosion of the investigated materials. Since As is a common impurity of Sb, it is of great interest to research its influence on material compatibility.

The results of post-test analysis show that all Fe-based alloys suffered from strong corrosion attack at 450 °C in Sb_3Sn_7, although for none of the Fe-based alloys the As impurity was found to play a significant role in the corrosion process. The As content declines towards the corrosion front. Highest As concentrations were found in the Cr-rich precipitates close the surface of the austenitic steels SS316L and SS304. This agrees with the strong affinity between Cr and As demonstrated by the calculated values of the enthalpy of formation for CrAs (47 kJ/mol) compared with CrSb (9 kJ/mol) or CrSn (3 kJ/mol) [42]. Because these precipitates do not form a continuous layer, they are not expected to have any influence on the corrosion process at the corrosion front. Kovar alloy, not containing any Cr, does not accumulate any As from the contaminated Sb-Sn alloy.

Besides As, also the oxygen impurity in the system could influence the corrosion/oxidation process in liquid Sb_3Sn_7. The determined water vapor to hydrogen ratio in the range 0.002 to 0.02 respectively oxygen partial pressure of 10 ^{36} to 10 ^{34} bar is too low to oxidize elements such Fe, Ni, Co, Mo, Sn, Sb, or As. However, the value is above the oxidation potential of Cr/Cr_2O_3 and well above the oxidation potential of Al/Al_2O_3. Although from a thermodynamic point of view Cr could be oxidized, the kinetics of oxide formation at such low oxygen potentials and temperatures is typically too slow to form a protective surface oxide and to prevent liquid metal corrosion (dissolution, penetration). Indeed, except for a slight oxidation of the specimen cross-sections after preparation, no oxygen was found in the corroded regions of the metallic samples, in particular no continuous and protective oxide layer was
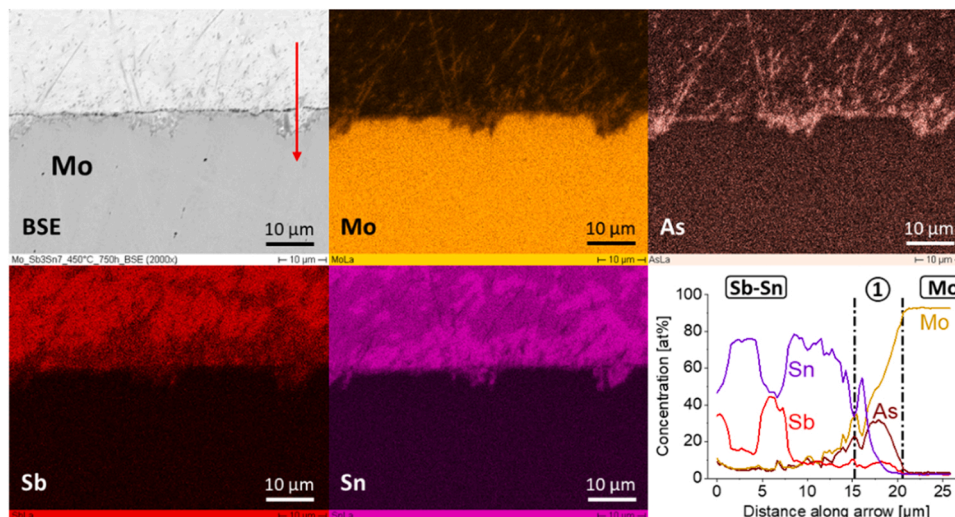

Fig. 11. Analysis of Mo after exposure in liquid Sb_3Sn_7 at 450 °C at higher magnification: BSE-SEM image, elemental mapping, and composition along red arrow.
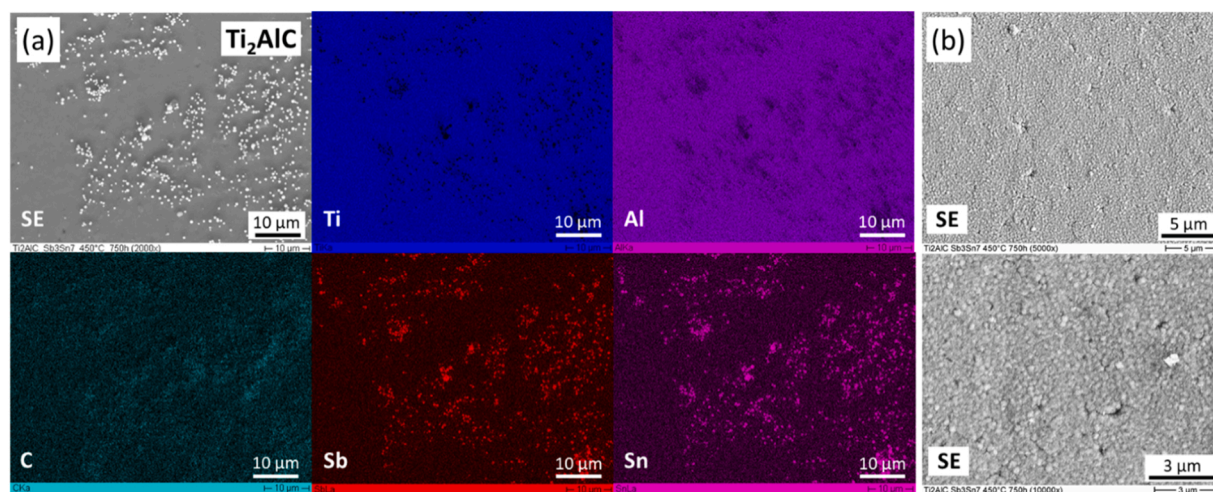
Fig. 12. Surface morphology of Ti$_2$AlC on Al$_2$O$_3$-substrate after 750 h exposure in liquid Sb$_3$Sn$_7$ at 450 °C: (a) SE-SEM image and EDS element mapping images, (b) SE-SEM images with higher resolution.

formed at the sample surfaces. Thus, the experimental results confirm that the amount of oxygen in the Sb-Sn alloy during exposure was low enough to mimic the oxygen-free case respectively a situation without continuous oxygen supply as found in an LMB cell. This does not apply for the MAX-phases due to their high Al content, see below.

The maximum corrosion rates of the Fe-based alloys range from 0.5 μm/h for T91 and 4J29 Kovar to 0.8 μm/h for SS316L respectively 1.3 μm/h for SS304. The corrosion rates of the steels in the present study are comparable with the average corrosion rates found after 160 h at 500 °C in Sb$_4$Sn$_6$ (~0.5 μm/h for SS304 and ~0.6 μm/h for SS316L) [26]. In both the cited and the present study, the corrosion layer facing the Sb-Sn alloy mainly consists of the intermetallic compound FeSb$_2$, while the corrosion layer adjacent to the steel has a much lower Sb content and is enriched in Cr. The higher corrosion rates of Fe-Cr-Ni steels (SS316L and SS304) compared with the Fe-Cr steel (T91) in the present study confirm the detrimental effect of Ni on the corrosion behavior found in previous studies [11,26]. The comparison of the results of SS316L in liquid Sb$_3$Sn$_7$ at 450 °C (max. corrosion rate 0.80 μm/h) with previously reported results of SS316L in liquid tin at 450 °C (max. corrosion rate more than 2 μm/h) [22] supports the expectation that pure Sn is even more aggressive towards steels than an Sb-Sn alloy.

Among the tested metallic bulk materials, only Mo metal shows a corrosion rate of less than 0.1 mm/a in Sb$_3$Sn$_7$. Except for very localized corrosion attacks due to the As contamination, Mo possesses an outstanding corrosion resistance during the exposure in Sb$_3$Sn$_7$ alloy at 450 °C. Even with the action of the As impurity, the corrosion rate after 750 h stays below 0.007 μm/h (0.06 mm/a). This agrees with previous studies [16,20,25], which regarded Mo as corrosion-resistant against liquid tin. However, it does not agree with recent corrosion results in liquid Sb$_4$Sn$_6$, which showed a Mo-Sb-Sn corrosion layer of ~50 μm thickness already after 500 h at 500 °C [27]. This corrosion layer was composed of ~50 at% Sb, ~30 at% Mo, ~10 at% Sn, and ~10 at% O. After 2000 h exposure, an average corrosion rate of 0.008 μm/h was deduced from the Mo matrix recession, which seems strongly reduced compared with the result after 500 h and is much closer to the observation of the present study.

With regards to the MAX-phase coatings, the surfaces of all three types of MAX-phases (Cr$_2$AlC, Ti$_2$AlC, and Ti$_3$AlC$_2$) coated on Al$_2$O$_3$-substrates are decorated by drops of Sb-Sn alloy after 750 h exposure to oxygen-poor liquid Sb$_3$Sn$_7$ at 450 °C. Neither destruction of the MAX-phases nor penetration of Sb-Sn alloy can be observed. The surfaces of all three MAX-phases maintain smooth and intact after exposure. A slight oxygen enrichment is detected at the sample surfaces. Since an Al-

rich oxide layer already existed prior to the exposure to Sb-Sn due to the MAX-phase preparation process, this result neither indicates nor excludes oxide growth during exposure. Because of the slow kinetics of both Al-oxide layer formation and its destruction by dissolution at the given conditions (temperature, oxygen content), much longer exposure experiments are required to draw any definite conclusion. Furthermore, the promising corrosion resistance of MAX-phases in oxygen-poor Sb-Sn alloys cannot be directly transferred to oxygen-free conditions.

Finally, as for Mo, the in-situ corrosion in an operating LMB cell needs to be investigated before their application as positive current collector in a liquid metal battery. Here, Na-based cells promise better performance in terms of corrosion resistance than Li‖Sb–Sn cells due to the less reactive properties of Na compared with Li.

5. Conclusion

In summary, the results of our work reveal that the corrosion rates of Fe-based alloys (Fe-Cr steel, Fe-Cr-Ni steels, and Kovar alloy) are in the range 0.5 to 1.3 μm/h and, thus, unacceptably high for use in oxygen-poor or oxygen-free liquid antimony-tin alloy environment. The corrosion behavior of the steels is characterized by penetration of both Sb and Sn and a stepwise decline of the Fe content from the unaffected steels towards the liquid metal. At the corrosion front, the contents of Sb and Sn roughly mount up to the content of Fe, while the adjacent region is dominated by Sb and Fe in an atomic ratio of 2:1, indicating formation of the intermetallic compound FeSb$_2$. Arsenic from a very small (<0.1 at%) impurity of the Sb-Sn alloy accumulates in Cr-rich regions of the corrosion attack of the steels but seems to have no significant effect on the processes at the corrosion front. Molybdenum metal and the three tested MAX-phase coatings (Cr$_2$AlC, Ti$_2$AlC, and Ti$_3$AlC$_2$), on the other hand, present outstanding corrosion resistance against oxygen-poor liquid Sb$_3$Sn$_7$ at 450 °C in static exposures. Although the As drives some local corrosion attacks of Mo, the maximum corrosion rate remains below 0.1 mm/a. Therefore, Mo and MAX-phases are regarded as the most promising candidates to be applied as PCC material in liquid metal batteries that use an Sb-Sn alloy as positive electrode. Considering the higher price, coatings of those promising materials on a suitable substrate (conductive metallic materials, e.g., steel or alloys) might be the most economically reasonable and feasible method. In case of MAX-phases, the insulating properties of pre-existing surface oxides need to be investigated. Additionally, corrosion tests of Mo and MAX-phases in an LMB cell under cycling conditions are required.

CRediT authorship contribution statement

Müller Georg: Conceptualization, Funding acquisition. **Stüber Michael:** Supervision. **Tang Chongchong:** Resources, Writing – review & editing. **Weisenburger Alfons:** Conceptualization, Writing – review & editing. **Heinzel Annette:** Investigation, Writing – review & editing. **Fetzer Renate:** Investigation, Visualization, Writing – original draft. **Zhang Tianru:** Investigation, Writing – original draft.

Declaration of Competing Interest

The authors declare that they have no known competing financial interests or personal relationships that could have appeared to influence the work reported in this paper.

Data availability

Data will be made available on request.

Acknowledgments

Supplementary Material

Experimental results on stainless steel SS304 and on the two MAX-phases Ti_3AlC_2 and Cr_2AlC (PDF).

Appendix A. Supporting information

Supplementary data associated with this article can be found in the online version at doi:10.1016/j.corsci.2023.111797.

References

[1] Z. Yang, et al., Electrochemical energy storage for green grid, Chem. Rev. 111 (5) (2011) 3577–3613, https://doi.org/10.1021/cr100290v.

[2] P.H.J. Nardelli *et al.*, "Models for the modern power grid," European Physical Journal: Special Topics, vol. 223, no. 12. Springer Verlag, pp. 2423–2437, Oct. 01, 2014. doi: 10.1140/epjst/e2014–02219-6.

[3] K. Wang, et al., Lithium-antimony-lead liquid metal battery for grid-level energy storage, Nature 514 (7522) (2014) 348–350, https://doi.org/10.1038/nature13700.

[4] H. Li, K. Wang, S. Cheng, K. Jiang, High performance liquid metal battery with environmentally friendly antimony-tin positive electrode, ACS Appl. Mater. Interfaces 8 (20) (2016) 12830–12835, https://doi.org/10.1021/acsami.6b02576.

[5] M.S. Whittingham, "History, Evolution, and Future Status of Energy Storage," Proceedings of the IEEE, vol. 100, no. Special Centennial Issue, pp. 1518–1534, 2012, doi: 10.1109/JPROC.2012.2190170.

[6] W. Ding, et al., Multi-cationic molten salt electrolyte of high-performance sodium liquid metal battery for grid storage, J. Power Sources 553 (2023), 232254, https://doi.org/10.1016/j.jpowsour.2022.232254.

[7] H. Zhou, et al., A sodium liquid metal battery based on the multi-cationic electrolyte for grid energy storage, Energy Storage Mater. 50 (2022) 572–579, https://doi.org/10.1016/j.ensm.2022.05.032.

[8] T. Dai, Y. Zhao, X.H. Ning, R. Lakshmi Narayan, J. Li, Z. wei Shan, Capacity extended bismuth-antimony cathode for high-performance liquid metal battery, J. Power Sources 381 (2018) 38–45, https://doi.org/10.1016/j.jpowsour.2018.01.048.

[9] H. Kim, et al., Liquid metal batteries: past, present, and future, Chem. Rev. 113 (3) (2013) 2075–2099, https://doi.org/10.1021/cr300205k.

[10] T. Ouchi, D.R. Sadoway, Positive current collector for Li||Sb-Pb liquid metal battery, J. Power Sources 357 (2017) 158–163, https://doi.org/10.1016/j.jpowsour.2017.04.104.

[11] K. Cui, et al., Feasibility research of SS304 serving as the positive current collector of Li||Sb-Sn liquid metal batteries, J. Phys. Chem. C 125 (1) (2021) 237–245, https://doi.org/10.1021/acs.jpcc.0c09629.

[12] J.R. Weeks, Lead, bismuth, tin and their alloys as nuclear coolants, Nucl. Eng. Des. 15 (1971) 363–372, https://doi.org/10.1016/0029-5493(71)90075-6.

[13] J. Pacio, Th Wetzel, Assessment of liquid metal technology status and research paths for their use as efficient heat transfer fluids in solar central receiver systems, Sol. Energy 93 (2013) 11–22, https://doi.org/10.1016/j.solener.2013.03.025.

[14] A. Fritsch, J. Flesch, V. Geza, Cs Singer, R. Uhlig, B. Hoffschmidt, Conceptual study of central receiver systems with liquid metals as efficient heat transfer fluids, Energy Procedia 69 (2015) 644–653, https://doi.org/10.1016/j.egypro.2015.03.074.

[15] A. Heinzel, et al., Liquid metals as efficient high-temperature heat-transport fluids, Energy Technol. 5 (7) (2017) 1026–1036, https://doi.org/10.1002/ente.201600721.

[16] R.N. Lyon, "Liquid-Metals Handbook," Washington 25, D.C.: Superintendent of Documents, U.S. Government Printing Office, Jun. 1952. Accessed: Oct. 19, 2022. [Online]. Available: https://www.osti.gov/biblio/4377939.

[17] G. Müller, A. Heinzel, G. Schumacher, A. Weisenburger, Control of oxygen concentration in liquid lead and lead–bismuth, J. Nucl. Mater. 321 (2) (2003) 256–262, https://doi.org/10.1016/S0022-3115(03)00250-2.

[18] J.-B. Vogt, I. Proriol Serre, A review of the surface modifications for corrosion mitigation of steels in lead and LBE, Coatings 11 (1) (2021), https://doi.org/10.3390/coatings11010053.

[19] W. Timmerhoff, Die Löslichkeit verschiedener Stähle ın Bleischmelzen, Int. J. Mater. Res. 34 (5) (1942) 102–104, https://doi.org/10.1515/ijmr-1942-340503.

[20] L.R. Kelman, W.D. Wilkinson, and F.L. Yaggee, Resistance of materials to attack by liquid metals. Argonne, IL (United States), 1950. doi: 10.2172/4419134.

[21] A. Weisenburger, F. Lang, G. Müller, Material and experimental issues related to the use of liquid metals as heat transfer media for CSP tower receivers, AIP Conf. Proc. 2033 (1) (2018) 80005, https://doi.org/10.1063/1.5067094.

[22] A. Heinzel, A. Weisenburger, G. Müller, Corrosion behavior of austenitic steel AISI 316L in liquid tin in the temperature range between 280 and 700 °C, Mater. Corros. 68 (8) (2017) 831–837, https://doi.org/10.1002/maco.201609211.

[23] T. Emmerich, C. Schroer, Corrosion in austenitic steels and nickel-based alloys caused by liquid tin at high temperature, Corros. Sci. 120 (2017) 171–183, https://doi.org/10.1016/j.corsci.2017.02.025.

[24] A. Heinzel, et al., Liquid metals as efficient high-temperature heat-transport fluids, Energy Technol. 5 (7) (2017) 1026–1036, https://doi.org/10.1002/ente.201600721.

[25] E.L. Reed, Stability of refractories in liquid metals, J. Am. Ceram. Soc. 37 (3) (1954) 146–153, https://doi.org/10.1111/j.1151-2916.1954.tb14013.x.

[26] W. Liu, H. Yin, K. Du, B. Yang, D. Wang, Corrosion behaviors of iron, chromium, nickel, low-carbon steel, and four types of stainless steels in liquid antimony-tin alloy, Corrosion 77 (11) (2021) 1192–1202, https://doi.org/10.5006/3820.

[27] K. Cui, et al., Stable positive current collectors for Li||Sb–Sn liquid metal batteries, ACS Appl. Energy Mater. 4 (9) (2021) 9013–9021, https://doi.org/10.1021/acsaem.1c01280.

[28] O.M. Akselsen, Review advances in brazing of ceramics, J. Mater. Sci. 27 (1992) 1989–2000, https://doi.org/10.1007/BF01117909.

[29] M.B. Uday, M.N. Ahmad-Fauzi, A.M. Noor, S. Rajoo, Current issues and problems in the joining of ceramic to metal. Joining Technologies, InTech,, 2016, https://doi.org/10.5772/64524.

[30] E.N. Hoffman, D.W. Vinson, R.L. Sindelar, D.J. Tallman, G. Kohse, M.W. Barsoum, MAX phase carbides and nitrides: properties for future nuclear power plant in-core applications and neutron transmutation analysis, Nucl. Eng. Des. 244 (2012) 17–24, https://doi.org/10.1016/j.nucengdes.2011.12.009.

[31] N.C. Ghosh, S.P. Harimkar, 3 - Consolidation and synthesis of MAX phases by spark plasma sintering (SPS): a review, Adv. Sci. Technol. (2012) 47–80, https://doi.org/10.1533/9780857096012.47.

[32] A. Heinzel, A. Weisenburger, G. Müller, Long-term corrosion tests of Ti3SiC2 and Ti2AlC in oxygen containing LBE at temperatures up to 700 °C, J. Nucl. Mater. 482 (2016) 114–123, https://doi.org/10.1016/j.jnucmat.2016.10.007.

[33] T. Lapauw, et al., Interaction of Mn+1AXn phases with oxygen-poor, static and fast-flowing liquid lead-bismuth eutectic, J. Nucl. Mater. 520 (2019) 258–272, https://doi.org/10.1016/j.jnucmat.2019.04.010.

[34] C. Tang, et al., Textured growth of polycrystalline MAX phase carbide coatings via thermal annealing of M/C/Al multilayers, J. Vac. Sci. Technol. A 38 (1) (2020) 13401, https://doi.org/10.1116/1.5131544.

[35] H. Shi, et al., Corrosion behavior of Al-containing MAX-phase coatings exposed to oxygen containing molten Pb at 600 °C, Corros. Sci. 201 (2022), 110275, https://doi.org/10.1016/j.corsci.2022.110275.

[36] X. Zhang, S. Friedrich, B. Friedrich, Separation behavior of arsenic and lead from antimony during vacuum distillation and zone refining, J. Mater. Res. Technol. 9 (3) (2020) 4386–4398, https://doi.org/10.1016/j.jmrt.2020.02.063.

[37] G. Coen, J. van den Bosch, A. Almazouzi, J. Degrieck, Investigation of the effect of lead-bismuth eutectic on the fracture properties of T91 and 316L, J. Nucl. Mater. 398 (1–3) (2010) 122–128, https://doi.org/10.1016/j.jnucmat.2009.10.021.

[38] C. Tang, et al., Textured growth of polycrystalline MAX phase carbide coatings via thermal annealing of M/C/Al multilayers, J. Vac. Sci. Technol. A 38 (1) (2020), 013401, https://doi.org/10.1116/1.5131544.

[39] C. Tang, et al., Synthesis and characterization of Ti2AlC coatings by magnetron sputtering from three elemental targets and ex-situ annealing, Surf. Coat. Technol. 309 (2017) 445–455, https://doi.org/10.1016/j.surfcoat.2016.11.090.

[40] H. Okamoto, M.E. Schlesinger, and E.M. Mueller, Eds., ASM Handbook, Volume 3: Alloy Phase Diagrams. ASM International, 2016. doi: 10.31399/asm.hb. v03.9781627081634.

[41] V. Raghavan, Fe-Sb-Sn (iron-antimony-tin), J. Phase Equilibria 22 (6) (2001) 669–670, https://doi.org/10.1007/s11669-001-0035-9.

[42] F.R. de Boer, R. Boom, A.R. Miedema, Enthalpies of formation of liquid and solid binary alloys based on 3d metals: II alloys of chromium and manganese, Phys. B+ C. 113 (1) (1982) 18–41, https://doi.org/10.1016/0378-4363(82)90107-3.